Impedance-Based AC/DC Terminal Modeling and Analysis of the MMC-BTB System

Chongbin Zhao [iD], *Student Member, IEEE*, and Qirong Jiang [iD]

Abstract—Impedance-based small-signal stability analysis is widely applied in practical engineering with modular multilevel converters (MMCs). However, the deficiencies of existing impedance models (IMs) and the idealized extension for the single MMC influence the analyses in multiterminal systems. In this article, these gaps are filled by focusing on an MMC-based back-to-back system. To obtain the steady-state harmonics of the system, a numerical method is initially proposed based on Newton–Raphson iteration in the frequency domain. Then, by substituting the shared terminal dynamics with active or passive devices, theoretical AC/DC IMs based on typical control loops with pure time delays are directly established via multiharmonic linearization. Further aided by the derived IMs, two neglected aspects in the current literature are investigated, including the influence of power transformers on low-frequency impedance characteristics and the rationality of using simplified IMs for high-frequency resonance studies. The stability of interlinking systems needs to be comprehensively analyzed at both AC and DC terminals. The analyses help to position the instability source, obtain the stability margin, and guide the supplementary control strategy. All IMs and analyses are verified via frequency scans and simulations in PSCAD.

Index Terms—Back-to-back system, impedance model, modular multilevel converter, stability analysis, steady-state harmonic.

NOMENCLATURE

Abbreviations

MMC	Modular multilevel converter.
TL-VSC	Two-level voltage source converter.
BTB	Back-to-back.
PS/NS/ZS	Positive-/negative-/and zero-sequence.
DM, CM	Differential- and common-mode.
IM, AM	Impedance and admittance model.
TIM/AIM	Theoretical and analytical impedance model.
CCSC	circulating current suppressing control.
ZSCC	Zero-sequence current control.
SE, NE	Sending and receiving end.

FFT	Fast Fourier transform.
1-d, 2-d	One- and two-dimensional.
eig, LR	Eigenvalues of an open-loop IM ratio.

Expressions

$G(x, y)$	Element of coordinates (x, y) of $(2n+1)$th order Toeplitz matrix G formed by Fourier vector g.
$(g/\Delta g)\langle i \rangle$	ith harmonic component of $(2n+1)$th $(g/\Delta g)$.
$a_{g\langle i \rangle}+b_{g\langle i \rangle}j$	Fourier coefficients of $g\langle i \rangle$.
$h(s)$	Transfer function.

Parameters and Variables

U, O	Identity and zero matrices.
C, L, R	Capacitance, inductance, and resistance.
P, Q, S	Active, reactive, and apparent power.
Y, Z	Admittance and impedance.
θ, ω, f	Angle, angular frequency, and frequency.
i, m, v	Variable of current, insertion index, and voltage.
d, q	Variable of outer loop dynamics in *dq*-frame.
n, N	Number of truncated harmonic order of vectors and submodule of each arm.
k, T	Unitary-proportional gain and time constant.

Prefix

Δ	Small-signal perturbation.

Subscripts

a, b, c	Variable of each phase in the stationary frame.
d, q, z	Direct-, quadrature-axis, and DC components in synchronous rotating frame.
b, RMS, pu	Base, root mean square, and per-unit value.
dc, g	DC and infinite grid terminal.
de, d, f, m, o	Coefficient/transfer function of decoupling, delay, feedforward, normalization, and offset.
v/w, a, c, ma	Transformer primary/secondary winding, turns-ratio, coupling and magnetizing coefficient.
p, 0, ..., n	Perturbation, DC, ..., n times line-frequency.
s, r	Sending and receiving end.
u, l	Upper and lower arm.

Superscripts

b	Base value.
c, d	Common- and differential-mode component.
p/n/z	Positive-/negative-/zero-sequence component.
*	Reference or rated value.
′, ″	Revised coefficient, matrix, and element.
0	Initial value for Newton–Raphson iteration.

I. INTRODUCTION

MMC-BASED multiterminal systems, featuring decoupled power control, good adaptability to various voltage levels, and high power quality [1], are expected to be widely applied in modern power systems. However, the recent real-world events, i.e., the 30 Hz subsynchronous oscillation [2] of the Nan-Ao wind power transmission project and the 1.2/0.7 and 1.8 kHz high-frequency oscillation [3], [4] of the Luxi/Yu-E grid interconnection project, attract broad concern for the system wideband harmonic stability issues, where the impedance-based method provides straightforward physical insights into the mechanism, protects the privacy of vendors, and can be validated via field tests.

Establishing the IM/AM that contains MMC is the basis of theoretical stability analysis, and extensive progress is reported in [2], [3], [4], [5], [6], [7], [8], [9], [10], [11], [12], [13], [14], [15], [16], [17], [18], [19], [20]. IM describes the ratio of the small-signal response of voltage and current at each frequency of interest. Toward a typical linear time-periodic system, IMs can be indirectly and directly derived based on the 1) harmonic state-space in the time domain [2], [3], [4], [5], [6], [7], [8], [9], [10] and 2) multiharmonic linearization in the frequency domain [11], [12], [13], [14], [15], [16]. Regarding the nonignorable control delay of the MMC, determination of a proper approximation order requires trial and error with ordinary differential equations [5], [6], [7], [9] for harmonic state-spaces, and even if great progress is made in [10] where the use of delay differential equations avoids the linearization of irrational transfer functions, the computation complexity is still high. Comparatively, the multiharmonic linearization sidesteps the flaws by eliminating intermediate variables and performing low-order matrix manipulation, and TIMs instead of AIMs that are common for TL-VSCs [17], [18], [19] are available (frequency responses are available for both TIM and AIM while explicit transfer functions are only available for AIM). Hence, multiharmonic linearization is intuitive since IMs/AMs are frequency domain models and the theoretical basis of this article.

In summary, studies were mostly focused on a single MMC in earlier research [2], [3], [4], [6], [8], [9], [10], [11], [16], [20], where ideal DC/AC voltage sources were deliberately assumed in general. The simplification diverged from the real world and led to the low credibility of the obtained AC/DC IMs on stability identification; thus, a generalized IM framework is needed that simultaneously considers both AC and DC terminal dynamics, which is not yet unified. In addition, only the ideal transformer model was included in the existing IMs where the mutual coupling was disregarded.

In addition to the aforementioned imperfections of IMs for the single MMC, more issues are noteworthy when combining separate IMs for multiterminal stability analysis. Initially, analytically computing the steady state in the time [21] or energy domain [22] with truncated harmonics considered with several simplifications, e.g., neglecting the active power loss or power flow constraints, is unreliable, while the measurement-based method [11] performed in the frequency domain is invalid when systems are unstable, and the inaccuracy of the steady

state impacts the IMs. Moreover, when the transformerless cases are focused on in the distribution network for flexible interconnection [23], the ZS DM impedance of an MMC-BTB system is no longer infinite as in the HVDC scenario, and the effect of virtual impedance on the stability induced by ZSCC is unclear. Finally, since the instability can arise from any of the AC and DC interconnections [13], [18], [19], it is essential to analyze the stability with detailed IMs rather than simplified IMs (the complete control loops are modeled in the detailed IM while several control loops are omitted in the simplified IM) at each terminal to position the authentic unstable modes or verify some deductions from TL-VSCs, which can also help show the core of some recent system-level stability analyses involving MMCs [24], [25]. Specifically, executing only DC stability analyses considering AC terminal dynamics [12] or vice versa [7] is not sufficient.

After determining the significance of facilitating the impedance-based stability analysis based on the satisfactory dynamic responses of systems, basic studies are completed by focusing on a three-phase symmetrical MMC-BTB system, which is a compromise between multiterminal and single MMC systems. This article aims to contribute the following.

1) Since multiharmonic linearization is performed in the frequency domain, a practical frequency domain steady-state computing method is proposed based on Newton–Raphson iteration, which covers the cases of whether transformers are configured and is compared with the existing methods.
2) Based on multiharmonic linearization, 1-d DC IMs are initially obtained, followed by sequence domain 2-d AC IMs fully considering the frequency coupling, typical control loops, pure time delays, and mutual coupling of transformers, whose accuracy is checked via frequency scans in PSCAD.
3) Aided by the derived accurate TIMs, sensitivity analyses are completed to clarify the influence on the stability of the nonideal transformer model and the virtual ZS DM impedance and to assess the rationality of the deduced simplified IM with line-frequency NS current (suppressing) control.
4) Using the 1-d Nyquist criterion at the DC terminal and the 2-d Nyquist criterion at the AC terminal, the utility of IMs is verified by correctly positioning the instability source under multiple operating conditions. The adaptivity of a decoupled 1-d Nyquist criterion [26] and the practical criterion proposed in [27] are also examined at the AC terminal.

The advantages of impedance-based modeling and analysis in this work are summarized as follows:

1) Compared with implementations by harmonic state-space, the treatment of pure time delay is straightforward and the adaptability to the practical "black-box" condition is high.
2) Among various impedance-based implementations, the procedure starting from a steady-state harmonic calculation is rigorous, enough unstable modes can be covered, and the extendibility can be confirmed.
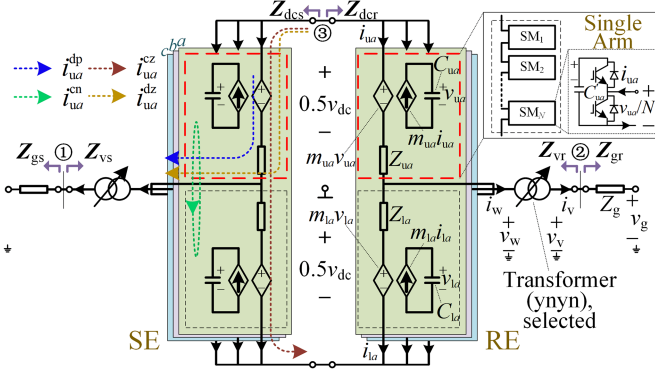
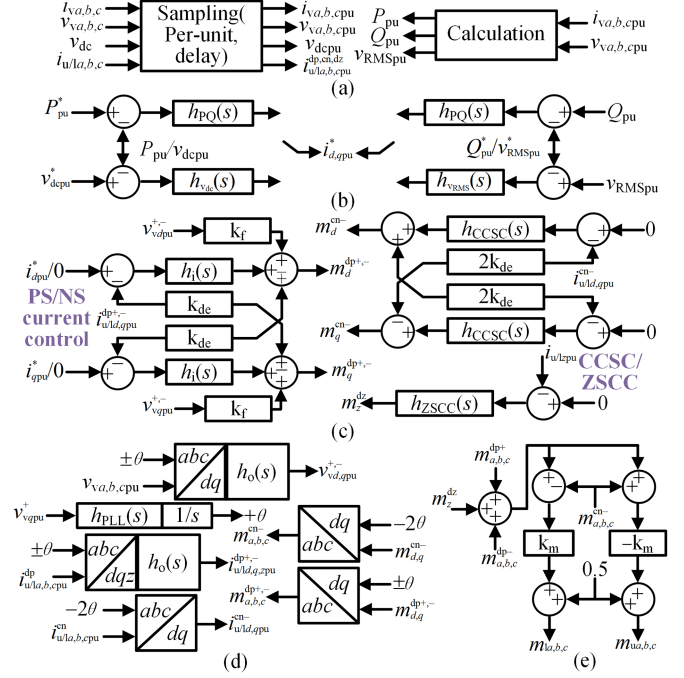Fig. 1. Diagram of the MMC-BTB system [3], [4].

Fig. 2. Control loops. (a) Processing. (b) Outer loop control. (c) Inner loop control. (d) (Inverse) Park transformation. (e) Insertion index generation.

The remainder of this article is organized as follows. Section II provides the elementary knowledge of the investigated system. A novel steady-state computing method is introduced in Section III, followed by the derivation and validation of TIMs in Section IV. Sensitivity and stability analyses are performed in Sections V and VI, respectively. Finally, Section VII concludes the work.

II. BASICS OF THE MMC-BTB SYSTEM

In this section, after introducing the configuration and control loops of the system in turn, the single-arm steady-state mathematical model is initially derived in the time domain and subsequently transformed to the frequency domain, which lays the foundation of the subsequent computing method and IMs. For conciseness, the ideal transformer model case is only provided in this section, and the nonideal transformer model or transformerless cases are comparatively discussed in Sections III and V.

A. Configuration

Fig. 1 shows the investigated MMC-BTB system based on the topology of real projects [3], [4]. Current paths and definitions of variables are briefly marked in phase a of SE&RE. The adopted average model for each arm indicates the following: 1) the submodule capacitance-voltage that belongs to the single arm is balanced and 2) the frequency range of concern is far below the equivalent switching frequency for stability analysis; these assumptions are generally acceptable according to existing studies. Since this article focuses on the modeling of MMCs under various control modes, the lumped parameters are adopted for the grid side for simplicity.

B. Control Loops

Referring to the most common grid-following control, the loops are illustrated in Fig. 2 referring to [4], [15]. Since MMC-BTB system is used to interconnect two AC networks in this study, the naming convention is centered around the AC system: the SE regulates P and Q and the RE regulates v_{dc} and v_{RMS} for outer loop control; NS current control and ZSCC are included

TABLE I
KEY PARAMETERS OF THE SYSTEM

Category	Symbol	Value (Unit)
Base	S_{b}, V_{gb}, V_{dcb}, f_1/T_1	10 MVA, 10 kV, 20 kV, 50 Hz/0.02 s
Grid	v_{gr}, v_{gs}	$10\angle 81°$, $11\angle 90°$
	L_{gr}, L_{gs}, R_{gr}, R_{gs}	10 mH, 0, 0, 2 Ω
MMC	L, R	50 mH, 0.5 Ω
	C', N	1000 μF, 20
Transformer	k_{a}, I_{ma}, X_{v}	1.25, 1%, 0.1 pu
Controller	P_{s}^*, Q_{s}^*, v_{dcr}^*, v_{RMSr}^*	5 MW, 0 MVA, 20 kV, 10 kV
	$h_{\text{PLL}}(s)$	$100+1/0.05s$
	$h_{\text{PQ}}(s)$, $h_{\text{vdc}}(s)$, $h_{\text{vRMS}}(s)$	$0.1+1/0.05s$, $4+1/0.05s$, $2+1/0.05s$
	$h_{\text{i}}(s)$, $h_{\text{CCSC}}(s)$, $h_{\text{ZSCC}}(s)$	$0.4+1/0.01s$, $0.8+1/0.01s$, $50+1/0.01s$
	T_{d}	300 μs

in addition to the regular PS current control and CCSC for inner loop control. T_{d} represents the sum of the control delay in the dq-frame, the sampling delay in the abc-frame is not considered, and the per-unit values are used for control. The key parameters are listed in Table I.

C. Single-Arm Time Domain Model

For the IM of a single MMC, by grasping the symmetric and periodic distribution of the internal multiharmonic variables, [11] introduces a focus on the single arm instead of the single phase [2], [6], [9]. Thus, this concept is extended to the BTB system. The dynamics of the upper arm, i.e., phase a of RE, can be reflected in the time domain:

$$\begin{cases} L(\mathrm{d}i/\mathrm{d}t) + Ri = 0.5v_{\text{dc}} - v_{\text{w}} - mv - v^{\text{dz}} \\ C(\mathrm{d}v/\mathrm{d}t) = mi, C = C'/N \end{cases} \tag{1}$$

where the subscript "uar" is neglected for simplification unless specified. v^{dz} is the voltage between the grounding and neutral point and acts as the source of the ZS DM circuit. An additional equation for the ideal transformer model is:

$$v_w = [v_v + L_v(\mathrm{d}(2i_{ua}^{dp}/k_a)/\mathrm{d}t)]/k_a \qquad (2)$$

Substituting (2) into (1) eliminates v_w and retains v_v and i, matching the demands of the voltage sampling in Fig. 2 and the arm current decomposition of deriving IMs.

D. Frequency Domain Interpretation

By replacing the time domain variable multiplication with the vector convolution and matrix-vector multiplication both in the frequency domain [11], (1) and (2) are converted to:

$$\begin{cases} i = Y_{LR}(0.5v_{dc} - v_v/k_a - Mv - v^{dz}) \\ Y_C v = Mi \end{cases} \qquad (3)$$

Y_{LR} and Y_C are diagonal transfer function matrices:

$$Y_{LR} = \mathrm{diag}\{[s + \mathrm{j}(x - 1 - n)\omega_1]L + R\}^{-1}$$
$$+ \mathrm{diag}\{h \cdot 2/k_a^2 \cdot 0.5(1+g)\{[s + \mathrm{j}(x-1-n)\omega_1]L_v\}\}^{-1},$$

$$Y_C = \mathrm{diag}\{[s + \mathrm{j}(x - 1 - n)\omega_1]C\}, 1 \le x \le 2n + 1,$$

$$h = \mathrm{sign}\{\mathrm{mod}[(x+2-n), 6]\}, g = 2\mathrm{mod}[(x-1-n), 2] - 1. \qquad (4)$$

Hence, v_v, m, i, and v are the steady-state vectors to be solved and form the corresponding Toeplitz matrices in (3). v^{dz} induces the coupling of both ends and differs from the single MMC:

$$v^{dz} = -\sum_{t=s,r} \frac{[Y_{LRt} + 2/k_a^2 \cdot Y_{gt}](x, x) \cdot (Mv)_t \langle \pm 3 \rangle}{\sum_{t=s,r} [Y_{LRt} + 2/k_a^2 \cdot Y_{gt}](x, x)},$$

$$x = n + 1 \pm 3. \qquad (5)$$

Due to the transformer, h in (4) ensures that the admittance of the ZS DM circuit is zero, and v^{dz} can be removed from (3); thus, ZS decouples from PS or NS in the DM circuit. Such a treatment needs to be assessed in the transformerless case.

III. FREQUENCY DOMAIN STEADY-STATE COMPUTING METHOD OF THE MMC-BTB SYSTEM

The steady state of TL-VSCs may be analytically obtained based on the intuitive physical meaning; however, it is unrealistic for MMCs due to the multiharmonic feature. To this end, a numerical method (b) is proposed and compared with the measurement-based method (a) and simulation (c), as the standard) in this section.

A. Concept and Hypotheses

Solving the phase and amplitude of each order of harmonics for a time domain variable can be regarded as solving $a_{g\langle i \rangle}$ and $b_{g\langle i \rangle}$ of frequency domain vectors with $s = \mathrm{j}\omega_1$ ($j2\pi f_1$), $\mathrm{j}\omega_2$, ..., $\mathrm{j}\omega_n$. Several hypotheses are formulated as follows:
1) Supposing that the steady-state errors are omitted, the control objectives of both the inner and outer loops are
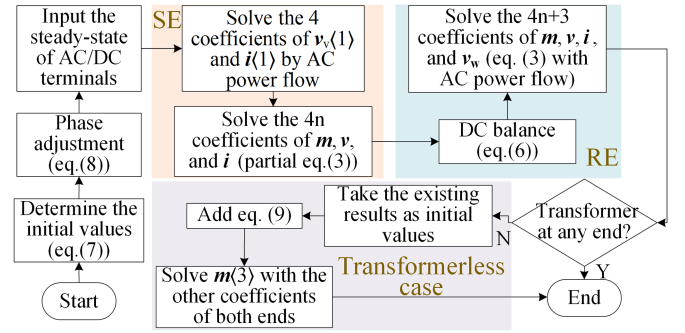

Fig. 3. Flow chart of the frequency domain steady-state computing method.

equal to their references, e.g., $v_{dc} = v_{dc}^* = v_{dcb}$; thus, v_{dc} becomes a known quantity.
2) Due to the conjugate relation between the $(n+1\pm i)$th elements of each vector, v introduces $(2n+1)$ unknowns; the use of CCSC and ZSCC/transformer causes $i\langle 2 \rangle$ and $i\langle 3 \rangle$ to be 0, and hence, i introduces $(2n-3)$ unknowns. Based on Fig. 2, $m\langle 0 \rangle = 0.5$ while $m\langle 1 \rangle$ (led by PS/NS current control), $m\langle 2 \rangle$ (led by CCSC), and $m\langle 3 \rangle$ (led by ZSCC) are nonzero; $v_v\langle 1 \rangle$ is related to the AC power flow and introduces two more unknowns. Thus, at most $(4n+6)$ equations are required for each end.
3) The iteration between v and i in (3) requires the truncation of each vector. Since $m\langle 3 \rangle$ is specifically focused, n is selected as 4 in this article.

B. Process and Annotations

A flow chart is provided to explain the process by first computing the coefficients of SE and subsequently RE, as shown in Fig. 3, and annotations are added as follows.
1) With the given P^*, Q^*, Z_g, and v_g, four coefficients contributed by $v_v\langle 1 \rangle$ and $i\langle 1 \rangle$ can be independently solved based on the AC power flow for SE. Suppose that the transformer is configured and $m\langle 3 \rangle = 0$; then, the remaining 4n coefficients of SE contributed by m, v, and i can be independently solved with the same number of real equations featured by the balance of $a_{g\langle i \rangle}$ and $b_{g\langle i \rangle}$ extracted from the matrix form of (3).
2) The DC balance holds for SE and RE:

$$v_{dcr}\langle 0 \rangle = v_{dcs}\langle 0 \rangle, i_r\langle 0 \rangle = -i_s\langle 0 \rangle. \qquad (6)$$

Equation (6) is satisfied because of the negligible electrical distance between the DC terminals in the grid interconnection scenario and can be adjusted if the voltage drop of DC line impedance needs to be considered in other scenarios. For RE, the remaining 4n+3 coefficients need to be simultaneously solved using the 4n equations from (3), two equations to represent the voltage drop of Z_{gr}, and an additional equation that represents the RMS voltage control.
3) The aforementioned nonlinear algebraic equations can be numerally solved via Newton–Raphson iteration, and part

TABLE II
COMPARISON BETWEEN CALCULATING METHODS OF THE SYSTEM
STEADY-STATE (UPPER ARM, PHASE A, TRANSFORMERLESS CASE)

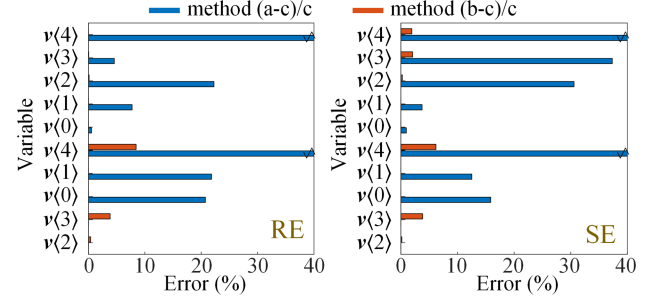| Variable	RE			SE		
	method a	method b	method c	method a	method b	method c
$v_v\langle 1\rangle$	10.00 0.00j	10.00 0.00j	10.00 0.00j	10.00 0.00j	10.00 0.00j	10.00 0.00j
$\boldsymbol{m}\langle 1\rangle$	−0.21 −0.050j	−0.21 −0.050j	−0.21 −0.050j	−0.20 0.052j	−0.20 0.052j	−0.20 0.052j
$\boldsymbol{m}\langle 2\rangle$	−0.0064 0.037j	−0.0072 0.037j	−0.0064 0.037j	−0.0082 −0.037j	−0.0079 −0.037j	−0.0082 −0.037j
$\boldsymbol{m}\langle 3\rangle$	$0(e^{-4})$ −0.026j	$0(e^{-4})$ −0.025j	$0(e^{-4})$ −0.026j	$0(e^{-4})$ −0.026j	$0(e^{-4})$ −0.025j	$0(e^{-4})$ −0.026j
$\boldsymbol{i}\langle 0\rangle$	0.099	0.082	0.082	−0.069	−0.082	−0.082
$\boldsymbol{i}\langle 1\rangle$	0.12 0.012j	0.099 0j	0.099 $0j(e^{-4})$	−0.086 −0.016j	−0.10 0j	−0.10 $0j(e^{-4})$
$\boldsymbol{i}\langle 2\rangle$	**0.021** **0.016j**	0 0j	$0(e^{-6})$ $0j(e^{-6})$	**0.022** **−0.017j**	0 0j	$0(e^{-6})$ $0j(e^{-6})$
$\boldsymbol{i}\langle 3\rangle$	**$0(e^{-4})$** **−0.0064j**	0 0j	$0(e^{-5})$ $0j(e^{-5})$	**$0(e^{-4})$** **0.0064j**	0 0j	$0(e^{-5})$ $0j(e^{-5})$
$\boldsymbol{i}\langle 4\rangle$	−0.044 −0.022j	−0.0061 0.0010j	−0.0057 $0j(e^{-4})$	−0.031 −0.019j	−0.0045 −0.0031j	−0.0048 −0.0033j
$v\langle 0\rangle$	20.55	20.44	20.44	20.46	20.66	20.66
$v\langle 1\rangle$	0.17 −2.17j	0.025 −2.02j	0.031 −2.02j	−0.20 2.06j	0.029 2.15j	0.029 2.15j
$v\langle 2\rangle$	0.25 0.46j	0.075 0.67j	0.068 0.67j	−0.090 −0.88j	0.088 −0.67j	0.10 −0.67j
$v\langle 3\rangle$	−0.022 −0.050j	−0.057 −0.0050j	−0.057 −0.0053j	0.081 −0.068j	−0.047 −0.063j	−0.047 −0.061j
$v\langle 4\rangle$	−0.22 0.45j	$0(e^{-4})$ 0.047j	$0(e^{-4})$ 0.047j	−0.19 0.30j	0.031 −0.025j	0.032 −0.025j

Fig. 4. Amplitude error of methods a and b compared with method c. The blue bar represents (method a-method c)/method c while the red bar represents (method b-method c)/method c.

of the initial values are given as (the rest are default to 0):

$$a^0_{\boldsymbol{v}_v\langle 1\rangle} = \sqrt{2}V_b/2\sqrt{3}, \; a^0_{\boldsymbol{m}_1\langle 1\rangle} = -2a^0_{\boldsymbol{v}_1\langle 1\rangle}/V_{dcb}, \; a^0_{\boldsymbol{v}\langle 1\rangle} = V_{dcb}. \tag{7}$$

4) When handling each coefficient for the calculation, a phase adjustment relative to $\boldsymbol{v}_v\langle 1\rangle$ is necessary:

$$a'_{\boldsymbol{g}\langle i\rangle} = \text{abs}(\boldsymbol{g}\langle i\rangle)\cos[\text{ang}(\boldsymbol{g}\langle i\rangle) - \text{ang}(\boldsymbol{v}_v\langle 1\rangle)],$$
$$b'_{\boldsymbol{g}\langle i\rangle} = \text{abs}(\boldsymbol{g}\langle i\rangle)\sin[\text{ang}(\boldsymbol{g}\langle i\rangle) - \text{ang}(\boldsymbol{v}_v\langle 1\rangle)],$$
$$\text{abs}(\cdot) = \sqrt{a^2_{(\cdot)} + b^2_{(\cdot)}}, \text{ang}(\cdot) = \arctan(b_{(\cdot)}/a_{(\cdot)}). \tag{8}$$

5) If the transformerless case is the focus, the above results can serve as the initials added with the addition of $a^0_{m(3)} = b^0_{m(3)} = 0$. With identical ZS circuit sampled and ZSCC for both ends, the follow-up (9) should be combined with the aforementioned $8n+3$ equations extracted from (3) for a simultaneous solution:

$$(\boldsymbol{Mv})_r\langle 3\rangle - (\boldsymbol{Mv})_s\langle 3\rangle = 0. \tag{9}$$

C. Validation

The steady-state harmonics of the transformerless case via the three methods with the operating conditions in Table I are listed in Table II the addition of and compared in Fig. 4. In Table II, the real and imaginary parts of each coefficient are listed in the upper and lower rows of each space. Fig. 4 shows that the overall error of proposed method b is much lower than that of method a even if some errors exist for $\boldsymbol{m}\langle 3\rangle$ and $\boldsymbol{i}\langle 4\rangle$, but their impact on the stability analysis is expected to be low.

In [11], $\boldsymbol{m}$ is initially obtained by simulation and then used in (3) to calculate $\boldsymbol{i}$ and $\boldsymbol{v}$ for method a; however, evident errors are observed, especially for $\boldsymbol{i}\langle 2\rangle$ which should theoretically be 0 due to CCSC, and $\boldsymbol{i}\langle 0\rangle$ as (6) indicates. Particularly, since $\boldsymbol{m}$ cannot be measured when the system is unstable, neither method a nor method c is rigorous, while the proposed method b has high precision and low computational overhead (normally, 4-6 iterations are adequate with proper initial values) and avoids the complicated but unnecessary transformation from the time or energy domain to the frequency domain [21], [22]. The magnitude of $\boldsymbol{m}\langle 3\rangle$ is nearly 70% of that of $\boldsymbol{m}\langle 2\rangle$ due to the nonexcessive L and C in the transformerless case that is possible for distribution networks. Considering the critical impact of CCSC on the stability [11], [12], it can be inferred ZSCC cannot be neglected in the IM if it is activated and will be elaborated on in Section V.

IV. DERIVATION OF AC/DC IMs OF THE MMC-BTB SYSTEM

The core work of developing IMs is introduced in this section. The modeling idea is clarified using the power stage and efforts are added to the control stage, whose transfer function matrices are provided in the Appendix for readability. DC and AC TIMs are then obtained and verified.

A. Basic Modeling Idea

There is a duality between AC and DC IMs, but it was not explicitly observed. Multiharmonic linearization of (3) yields:

$$\begin{cases} \Delta\boldsymbol{i} = \boldsymbol{Y}_{LR}(0.5\Delta\boldsymbol{v}_{dc} - \Delta\boldsymbol{v}_v/k_a - \boldsymbol{M}\Delta\boldsymbol{v} - \boldsymbol{V}\Delta\boldsymbol{m}) \\ \boldsymbol{Y}_C\Delta\boldsymbol{v} = \boldsymbol{M}\Delta\boldsymbol{i} + \boldsymbol{I}\Delta\boldsymbol{m} \end{cases} \tag{10}$$

$\Delta\boldsymbol{m}$ is closely related to the sampling and control as illustrated in Fig. 2:

$$\Delta\boldsymbol{m} = \boldsymbol{B}_{\boldsymbol{i}}\Delta\boldsymbol{i} + \boldsymbol{B}_{\boldsymbol{v}_v}\Delta\boldsymbol{v}_v + \boldsymbol{B}_{\boldsymbol{v}_{dc}}\Delta\boldsymbol{v}_{dc} \tag{11}$$

In this study, $\Delta\boldsymbol{v}$ does not contribute to $\Delta\boldsymbol{m}$ as Fig. 2 indicates, but if energy-based control is considered, an extra $\boldsymbol{B}_{\boldsymbol{v}}$ needs to be developed in (11). Since IM describes the relationship between selected elements of $\Delta\boldsymbol{i}$ with $\Delta\boldsymbol{v}_v$ or $\Delta\boldsymbol{v}_{dc}$, $\Delta\boldsymbol{m}$ and $\Delta\boldsymbol{v}$ are the intermediate variables and can be eliminated by combining (10) and (11). Moreover, an additional equation to eliminate $\Delta\boldsymbol{v}_v$ or $\Delta\boldsymbol{v}_{dc}$ for DC or AC IM is available since the dynamics can be

described from the two sides of each partition point in Fig. 1 based on Kirchhoff's voltage law. DC IMs are initially derived and subsequently used for deriving AC IMs.

Furthermore, two points are claimed: 1) AMs are first developed, followed by the inversion to IMs, and 2) since $s = j\omega_p$ of the IM corresponds to $s = j\omega_1$ of the steady-state, there is a position offset between two elements in $\Delta g\langle i\rangle$ and $g\langle i\rangle$ that hold the same CM-DM/sequence distribution law [11].

B. Control Stage

Eq. (11) is reformulated to (12) for the modeling modularity:

$$-\Delta m = J\Delta i + K\Delta v_v + E\Delta d + F\Delta q \qquad (12)$$

where J and K describe the influence of the inner loop control on Δm from Δi and Δv_v with the fixed reference values; Δd and Δq cooperate with E and F to reflect the influence of the outer loop control on Δm without the inner loop control.

Since $\Delta v_v = 0$ ensures $\Delta\theta = 0$, a process of current sampling, (inverse) Park transformation, and linear control ensures Q a diagonal matrix. P is related to the feedforward and phase-locked loop (PLL), where the former is similar to Q and the latter introduces off-diagonal terms. The closed-loop PLL transfer function considering multiple delays reflected by h_o ($T_1/4$ phase-shift offset) and h_d (aggregated control delay) is:

$$h_{\text{PLL}}(s) = \frac{\Delta\theta}{\Delta v_v\langle\pm 1\rangle} = e^{-\text{ang}(v_v\langle 1\rangle)}[h'_{\text{PLL}}(s)$$

$$+2\text{abs}(v_v\langle 1\rangle)]$$

$$h'_{\text{PLL}}(s + j\omega_1) = [k_v\cdot[h_o\cdot h_d](s)\cdot h_{\text{PLL}}(s)\cdot(1/s)]^{-1} \qquad (13)$$

Δd and Δq are dedicated by the control modes, whose relationships with sampling are described by matrices $U, R, S, T, W,$ and V. The cascade controllers are contained in E and F. Finally, $B_i, B_{vdc},$ and B_{vv} can be expressed with the aforementioned matrices.

C. Derivation and Validation of DC IM

Since i_{dc} is 3 times i_{ua}^{cz} while i_w is 2 times i_{ua}^{dp}, the extra equation to eliminate Δv_v for the 1-d DC AM/IM Y_{dc}/Z_{dc} is:

$$\Delta v_v = 2/k_a\cdot\underbrace{0.5(1+g)\text{diag}[(s+j(x-1-n)\omega_1)L_g]}_{Z_g(s)(x,x)}\Delta i,$$

$$x = n\pm 1 \qquad (14)$$

Substituting (11) and (14) into (10) gives:

$$Y_{dc} =$$

$$(3A_{dc}^{-1}B_{dc})_{[(n,n)]}, Z_{dc} = Y_{dc}^{-1}, B_{dc} = 0.5Y_CY_{LR} - BB_{v_{dc}},$$

$$A_{dc} = A + BB_i + 2/k_a\cdot Z_g(BB_{v_v} + Y_CY_{LR}),$$

$$A = Y_C + Y_{LR}M^2, B = Y_{LR}(MI + Y_CV). \qquad (15)$$

The accuracy of DC IMs of both ends is validated as shown in Fig. 5. The solid lines represent the theoretical IM by taking frequency of interest into (15), and the marks represent the frequency scans. Due to the sampling delay of v_{dc}, the passivity
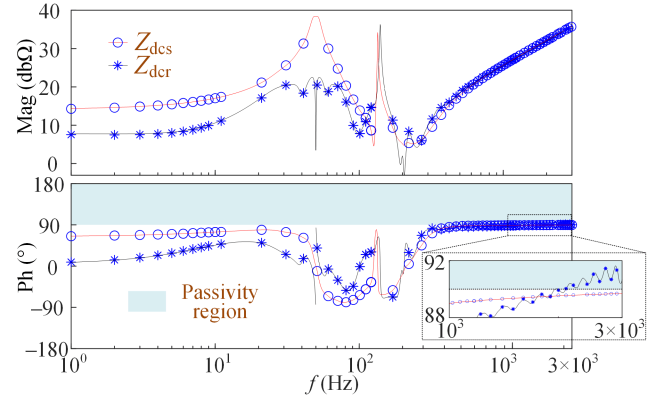

Fig. 5. Validation of DC IMs.

is introduced only for RE MMC at the high frequency as the zoom-in shows. A small 1 μs solution time step with a 50 μs sampling time is used in the frequency scan, which not only eliminates the majority of errors of discrete action toward the focused continuous IMs combined with the average model of MMC but also cover the 3 kHz maximum scanning frequency.

D. Derivation and Validation of AC IM

To derive the sequence domain 2-d AC AM/IM Y_v/Z_v, the following dual expression of (14) to eliminate Δv_{dc} is:

$$\Delta v_{dc} = -3\hat{Z}_{dc}\Delta i \qquad (16)$$

where "^" indicates that only the subscript s or r of Z_{dc} is inconsistent with that of the other matrices in (17):

$$Y_v =$$

$$(2/k_a\cdot A_v^{-1}B_v)_{\left[\begin{smallmatrix}(n+1,n+1) & (n+1,n-1)\\(n-1,n+1) & (n-1,n-1)\end{smallmatrix}\right]}, Z_v = Y_v^{-1},$$

$$B_v = (Y_CY_{LR})/k_a + BB_{v_v},$$

$$A_v = A + BB_i + (0.5Y_CY_{LR} - BB_{v_{dc}})\hat{Z}_{dc}/3. \qquad (17)$$

With the conjugate symmetry of 2-d Z_{ac} [5], only the two elements that belong to the same row are plotted for each end in Fig. 6, and the modeling accuracy is confirmed to be similar to that in Fig. 5. Since matrices $A, B, B_i, B_{vdc},$ and B_{vv} are shared in (15) and (17), there must be a generalized modeling framework for AC and DC IMs.

V. SENSITIVITY ANALYSIS

Since the derived IMs are based on (3) of the ideal transformer model in Section IV, the influence on IM of the nonideal transformer model and the case without transformers remain unclear. Detailed IMs can also serve as standards to check the errors of simplified IMs at high frequencies. Due to the pure time delay and the inverse of A_v or A_{dc} in AMs, AIMs are impractical, and sensitivity analyses are completed by adjusting key parameters and replotting TIMs point-by-point.
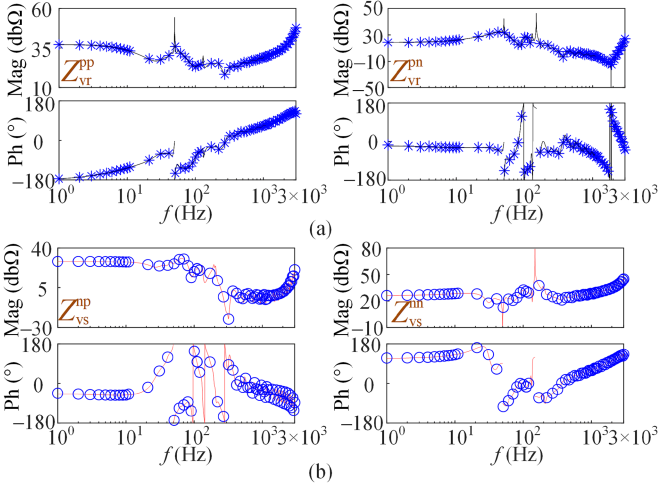
Fig. 6.   Validation of the AC IMs. (a) RE. (b) SE.
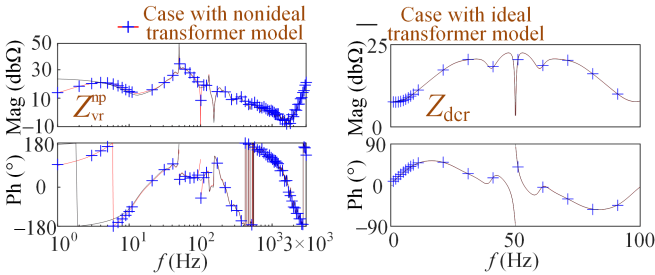

Fig. 7.   Influence on AC/DC IM of the nonideal transformer.

A. Issues of the Nonideal Transformer Model

The classical modeling approach of the nonideal transformer is based on the following frequency domain formula in PSCAD:

$$\begin{bmatrix} \boldsymbol{v}_\mathrm{v}\,\langle\pm1\rangle \\ \boldsymbol{v}_\mathrm{w}\,\langle\pm1\rangle \end{bmatrix} = s \begin{bmatrix} L_\mathrm{vv} & L_\mathrm{vw} \\ L_\mathrm{vw} & L_\mathrm{ww} \end{bmatrix} \begin{bmatrix} -i_\mathrm{v}\,\langle\pm1\rangle \\ i_\mathrm{w}\,\langle\pm1\rangle \end{bmatrix} \quad (18)$$

where L_vv, L_ww, and L_vw are the self-inductances of winding v/w and the mutual inductance. Thus, (2) of the ideal transformer model turns to (19) of the nonideal transformer model:

$$\boldsymbol{v}_\mathrm{v}\,\langle\pm1\rangle = (L_\mathrm{vw}/L_\mathrm{ww})\cdot\boldsymbol{v}_\mathrm{w}\,\langle\pm1\rangle - sL_\mathrm{vv}(1-k_\mathrm{c}^2)\cdot2\boldsymbol{i}\,\langle\pm1\rangle/\mathrm{k}_\mathrm{a},$$

$$2\boldsymbol{i}\,\langle\pm1\rangle/\mathrm{k}_\mathrm{a} = (L_\mathrm{vv}/L_\mathrm{vw})\cdot\boldsymbol{i}_\mathrm{v}\,\langle\pm1\rangle - \boldsymbol{v}_\mathrm{v}\,\langle\pm1\rangle/(sL_\mathrm{vw}),$$

$$\mathrm{k}_\mathrm{c} = L_\mathrm{vw}/\sqrt{L_\mathrm{vv}L_\mathrm{ww}}. \quad (19)$$

Based on k_a, I_ma, X_v, and S_b which are listed in Table I, k_c is 0.9995 while both $(L_\mathrm{vv}/L_\mathrm{vw})$ and $(L_\mathrm{vw}/L_\mathrm{ww})$ are close to k_a. Generally, the coupling between $\boldsymbol{i}_\mathrm{v}$ and $\boldsymbol{v}_\mathrm{v}$ in the second equation of (19) induces an extra negative impedance $\boldsymbol{Z}_\mathrm{vv}$ shunt connected with the deduced $\boldsymbol{Z}_\mathrm{ac}$ in (17), which mainly affects the low-frequency impedance characteristics of the AC IM and contradicts the simple handling in [12]. However, DC IM is almost unaffected since $\boldsymbol{Z}_\mathrm{vv}$ is far greater than $\boldsymbol{Z}_\mathrm{g}$. These inferences are supported as shown in Fig. 7, where the steady-state harmonics are recalculated considering (19), and the appropriate adjustments are given on control stages, e.g., replacing k_a to
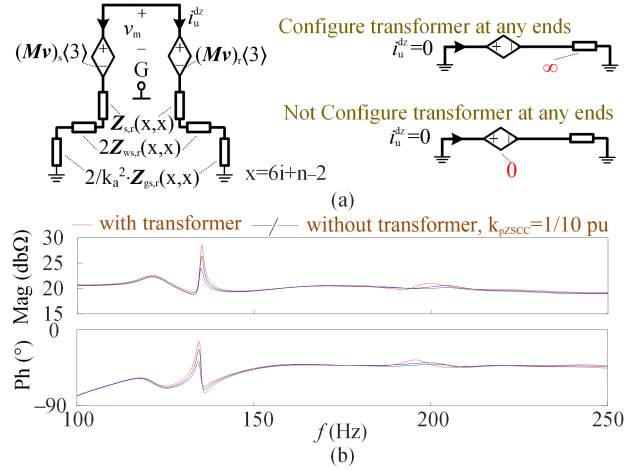

Fig. 8.   Influence on AC/DC IM whether any transformer is configured. (a) Diagrams of the principle of $i_{ua}^{dz} = 0$ for various cases. (b) 1-d PS Bode plots.

$(L_\mathrm{vv}/L_\mathrm{vw})$ and updating $\boldsymbol{B}_{\boldsymbol{v}\mathrm{v}}$ for both AC and DC IMs while further revising (17) for DC IMs.

B. Issues of the Transformerless Case

Since ZSCC is activated in the transformerless case, an extra submatrix is introduced for $\boldsymbol{J}$:

$$\boldsymbol{J}_3^\mathrm{z}(s)(\mathrm{x}, \mathrm{x}) = -0.5(1+g)\cdot h_\mathrm{d}(s+\mathrm{j}\omega_1)$$
$$\cdot[h_\mathrm{ZSCC}(s+\mathrm{j}(\mathrm{x}-3g)\omega_1)]\cdot2\mathrm{k}_\mathrm{m}\mathrm{k}_\mathrm{i}, \mathrm{x} = n\pm3. \quad (20)$$

With the computation of $\boldsymbol{m}\langle3\rangle$ in (9), the principle of $i_{ua}^{dz} = 0$ and $\boldsymbol{v}^\mathrm{dz}$ elimination is clarified in Fig. 8(a). The sufficient virtual impedance balance $\boldsymbol{Mv}\langle3\rangle$ with its small-signal $(\boldsymbol{M}\Delta\boldsymbol{v}+\boldsymbol{V}\Delta\boldsymbol{m})\langle3\rangle$ of two ends over the wideband by $h_\mathrm{ZSCC}(s)$ and h in (4) can be moved from $\boldsymbol{Y}_\mathrm{LR}$ to its product terms in $\boldsymbol{A}$ and $\boldsymbol{B}$. Hence, two more effects on IMs induced via ZSCC are 1) the change in $\boldsymbol{M}$ as Table II shows and 2) the release of $\boldsymbol{Y}_\mathrm{C}(\mathrm{x}, \mathrm{x})$, $\mathrm{x} = n+1\pm3$ in $\boldsymbol{A}_\mathrm{v}$, $\boldsymbol{B}_\mathrm{v}$, $\boldsymbol{A}_\mathrm{dc}$, and $\boldsymbol{B}_\mathrm{dc}$.

A 1-d positive sequence Z_v^p is transformed from 2-d $\boldsymbol{Z}_\mathrm{v}$ and $\boldsymbol{Z}_\mathrm{g}$ for a more intuitive analysis [26]:

$$Z_\mathrm{v}^\mathrm{p} = Z_\mathrm{v}^\mathrm{pp} - Z_\mathrm{v}^\mathrm{np}Z_\mathrm{v}^\mathrm{pn}/(Z_\mathrm{g}^\mathrm{nn} + Z_\mathrm{v}^\mathrm{nn}) \quad (21)$$

By comparing the transformer ($\mathrm{k}_\mathrm{a} = 1$, $X_\mathrm{v} = 0$) and transformerless cases in Fig. 8(b), a larger $\mathrm{k}_\mathrm{pZSCC}$ damps the resonant peaks over $3f_1$ to $5f_1$ and has a cumulative effect at the low frequency according to (3). In addition, the influence on the stability of 3rd harmonic injection to suppress the fluctuation of v [28] remains an open issue based on the conclusion of this subsection and is worthy of note.

C. Issues of High-Frequency Simplified IMs

PS AIMs are welcomed to design notch-filter-based or self-adaptive high-frequency oscillation suppressing control [4], [16], [20]. The proposed simplified AIM is provided in (22) with the following annotations:
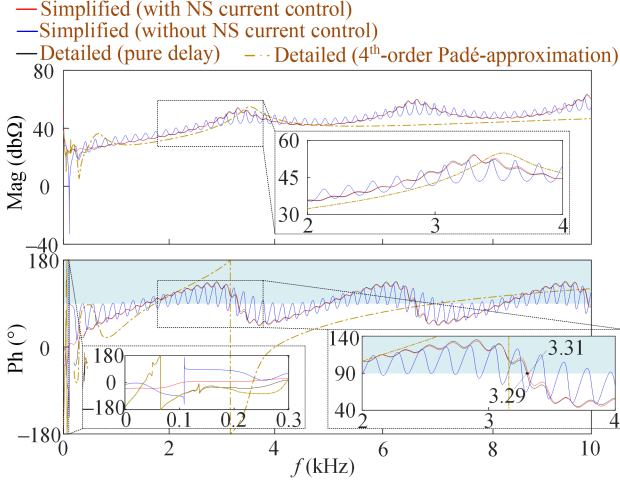
Fig. 9. Comparisons of AC IMs over the high-frequency.

Fig. 10. Definition of subsystems for stability analyses at various terminals.

1) With the limited bandwidth of outer-loop control, only the inner-loop current control and voltage feedforward are included, which is a consensus for high-frequency simplified IM. The coefficients k need to be elaborately managed based on the control loops in Fig. 2.

2) Distinguishing from the PS fundamental current control that a f_p/f_n ($f_n = f_p{-}2f_1$) perturbation results in a $f_p{-}f_1/f_n{+}f_1$ perturbation through Park transformation and then yielding a f_p/f_n response through inverse Park transformation, for the NS current control, a f_p/f_n perturbation results in a $f_p{+}f_1/f_n{-}f_1$ perturbation through Park transformation and finally a f_p/f_n response through inverse Park transformation; thus, the NS control should be fully modeled in (22) but is not fully considered for real project analysis in [4] or the related works in [15], [16], [17], [18], [19], [20].

3) Another critical observation is that $v\langle 0\rangle$ replaces $v_{dc}\langle 0\rangle$ since MMC uses v rather than v_{dc} for modulation, which confirms the necessity of steady-state calculation in Section III.

The rationality determination of the simplified AC IMs over the high frequency is reflected in Fig. 9. Whether NS current control is modeled or not in (22) shown at the bottom of this page, a nearly 20 Hz passivity region deviation or unacceptable errors due to the $T_1/4$ phase offset are observed, as the blue or red solid lines show. It is also the $T_1/4$ applied in the positive-negative sequence separation that leads to the periodic nature of several frequency responses in Fig. 9 [15] and can also be verified using (22). Furthermore, the 4th-order Padé approximation on a 300 μs pure time delay at multiple sampling paths is most effective below 200 Hz. Since the frequency responses are practical
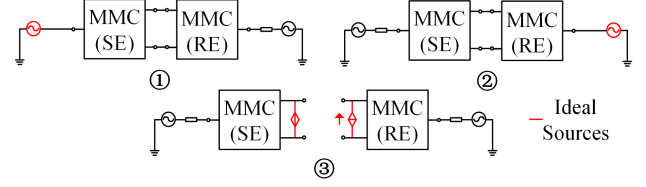
requirements for stability analysis, it is recommended to keep the preliminary irrational form e^{-sT} to correctly address the time delay over high frequency, as shown in this article and the former work [10].

VI. CASE STUDY

Three cases are studied in this section: the change in short-circuit ratio (a), the parameter tuning of $h_{vdc}(s)$ (b), and the step of P (c). Since some cases are not similar to those of the real world and the overhead lines are replaced by a lumped Z_g in particular, these studies predominantly verify the necessity and wideband accuracy of the TIMs. The simulation parameters are based on Table I without specification.

An alternative method to determine whether there is a right-half plane pole in the transfer function matrix LR is to examine whether the subsystems in Fig. 10 can stably operate through simulation. The LR of each terminal in Fig. 1 is defined as:

$$\text{①} - \text{SE}, \text{AC}(2-\text{d}): \boldsymbol{LR}_{vs} = \boldsymbol{Z}_{gs}\boldsymbol{Y}_{vs},$$
$$\text{②} - \text{RE}, \text{AC}(2-\text{d}): \boldsymbol{LR}_{vr} = \boldsymbol{Z}_{gr}\boldsymbol{Y}_{vr},$$
$$\text{③} - \text{DC}(1-\text{d}): \boldsymbol{LR}_{dc} = \boldsymbol{Z}_{dcr}\boldsymbol{Y}_{dcs}. \quad (23)$$

This method is acceptable in engineering since TIMs cannot directly provide system zeros and poles of MMC, which is emphasized to correctly apply the Nyquist criteria with frequency responses. Considering the conjugate symmetry of eig_p and eig_n for AC subsystems and the self-symmetry of eig_{dc} for the DC subsystem, the symmetries are both centered on f_1 for the sequence domain model, -2900 Hz to 3000 Hz of eig_p and 50 Hz to 3000 Hz of eig_{dc} with a step of 0.1 Hz are selected for the eigenvalue calculations.

A. Case A: Change in Short-Circuit Ratio

If the nonideal instead of the ideal transformer model is used and L_{gr} is increased from 22 mH to 25 mH (short-circuit ratio from 1.45 to 1.27), a diverged oscillation is first observed at $t = 4$ s and subsequently becomes a sustained oscillation for all of i_{vra}, i_{vsa} (with a very small harmonic amplitude), and i_{dc} in

$$Z_v^{p'} = \frac{k_a\{\underbrace{\boldsymbol{Z}_{LR}(n+2, n+2)}_{\text{Physical impedance}} + 2v\langle 0\rangle \cdot k_m k_i \cdot \{\underbrace{[h_i(s) - jk_{de}] \cdot [h_o \cdot h_d](s)}_{\text{PS current control}} + \underbrace{[h_i(s + j2\omega_1) + jk_{de}] \cdot [h_o \cdot h_d](s + j2\omega_1)]}_{\text{NS current control}}\}\}}{2\{1/k_a - \underbrace{v\langle 0\rangle \cdot k_m k_f k_v \cdot \{[h_o \cdot h_d](s) + [h_o \cdot h_d](s + j2\omega_1)\}}_{\text{PS/NS voltage feedforward}}\}} \quad (22)$$
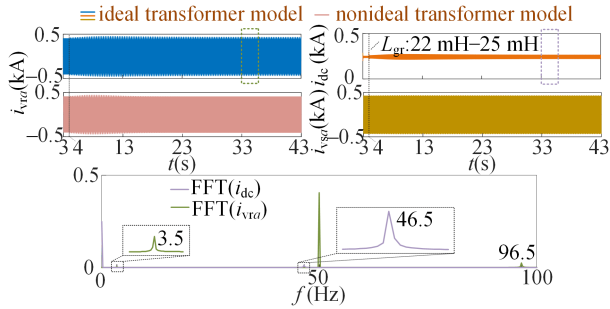
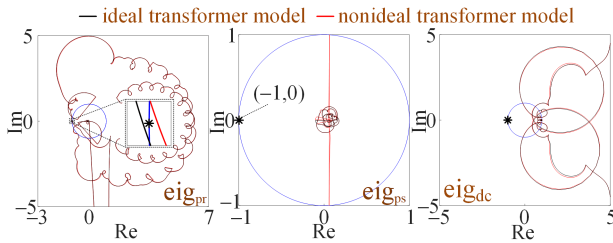Fig. 11.   Time domain simulation with the FFTs (case a).
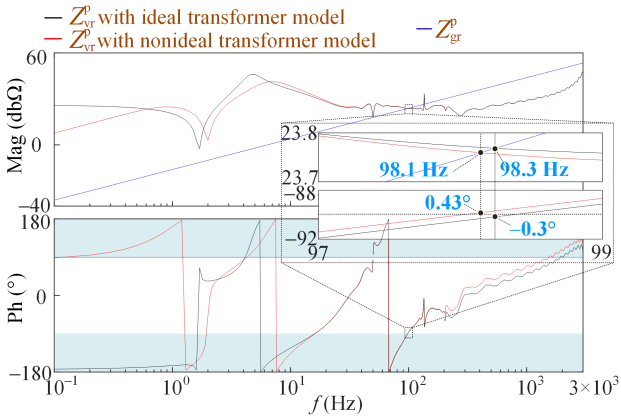

Fig. 12.   2-D Nyquist plots (case a).

Fig. 13.   1-D PS Bode plots (case a).

Fig. 11. The FFT shows that $|f_P-f_1| = 46.5$ Hz. Fig. 12 shows that only eig_{pr} of the nonideal transformer model judges an instability mode, whose model frequency (the initial oscillating frequency, a deviation with the sustained oscillation frequency is reasonable) and PM are approximately 98.2 Hz ($|f_P-f_1| = 48.2$ Hz) and –0.3°, respectively, aided by the equivalent 1-d PS Bode plot, as shown in Fig. 13.

The above theoretical analyses are consistent with the simulations; two deductions for case a are as follows: 1) using the ideal transformer model to deduce IM can omit the sub/super synchronous instability mode and 2) since the instability mode is only correctly identified at RE AC instead of SE AC or the DC terminal, a supplementary control should be added for RE related to its pure AC dynamics (e.g., PLL or inner-loop current control); even if DC voltage control also influences the AC
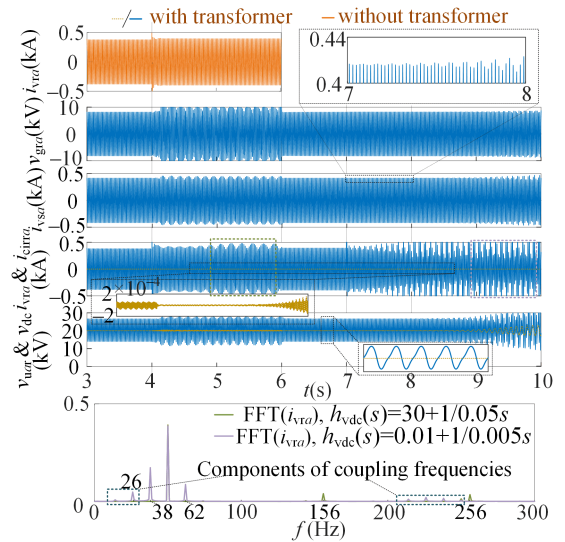

Fig. 14.   Time domain simulation with the FFTs (case b).

sub-super synchronous dynamic responses [7], it should not be given priority.

B. Case B: Tuning of $H_{vdc}(s)$

To ensure the universality of the conclusions in the last subsection, case b is studied, where the leakage inductance of the transformer is deliberately omitted to examine the necessity of Section V. B. A group of heuristic simulations is given for each subsystem, which has the time logic as follows:

1) At $t = 3$ s, L_{gr} is set to 0 and k_{pvdc} is set to 30; 2) At $t = 4$ s, L_{gr} becomes its rated value L_{gr}^* (10 mH); 3) At $t = 6$ s, k_{pvdc} becomes 4; 4) At $t = 7$ s, k_{pvdc} becomes 0.01, T_{ivdc} becomes 0.005, and L_{gr} becomes 0 again; 5) At $t = 8$ s, L_{gr} becomes L_{gr}^*. AC/DC terminal and arm capacitor voltages as well as the phase/circulating currents are shown in Fig. 14, and further simulations confirm that subsystem ② can stably operate whether the transformers are configured when $h_{vdc}(s) = 30+1/0.05s$ instead of $h_{vdc}(s) = 0.01+1/0.005s$; however, subsystem ① cannot stably operate with any controllers and subsystem ③ can stably operate with both controllers (the simulation is disregarded).

Furthermore, two instability cases are identified by eig_{dc} when L_{gr}^* is accessed to RE with transformers configured in Figs. 15 and 16, whose corresponding Bode plots match the FFTs in Fig. 14($|f_P-f_1| = 206$ Hz & 12 Hz). eig_{dc} also confirms the stable operation of the transformerless case with a PM of 1.15° when $h_{vdc}(s) = 30 + 1/0.05$ s. However, AC IMs cannot determine the instabilities that are induced by the improper h_{vdc} except eig_{pr} in Fig. 15 (two eig_ps are omitted and they cannot determine the instabilities).

The deductions on case b are: 1) the instabilities induced by the too large or too small k_{pvdc} reflect various system modes, and detailed IMs should be applied to correctly identify them; 2) the discussion in Section V.B is necessary, and the effect of
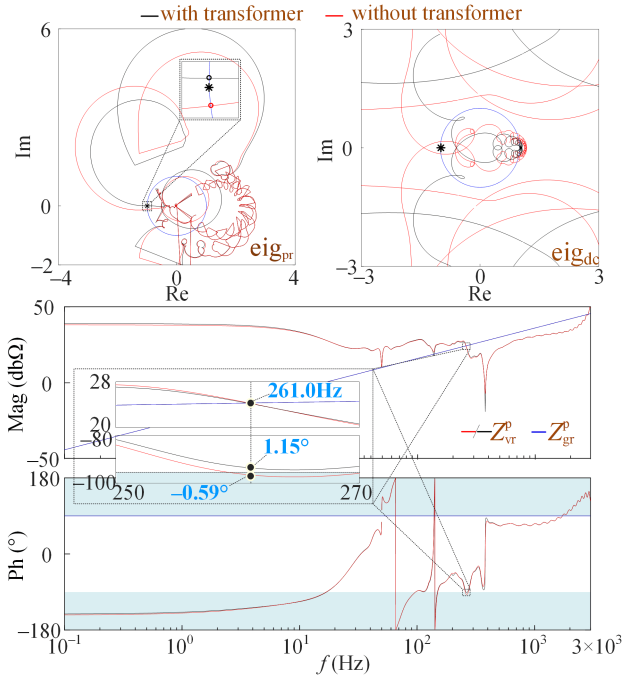
Fig. 15. Nyquist and Bode Plots ($h_{\text{vdc}}(s)=30+1/0.05\,s$).
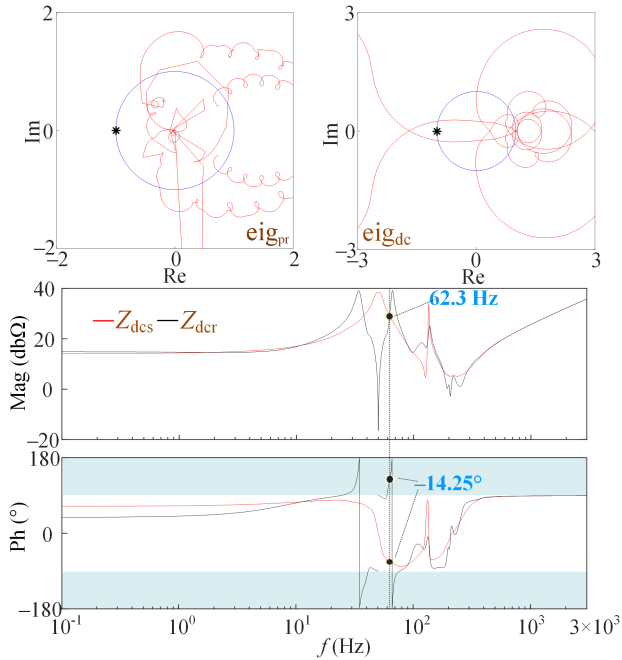
Fig. 16. Nyquist and Bode Plots ($h_{\text{vdc}}(s) = 0.01+1/0.005\,s$).

ZSCC on the stability over $3f_1$ to $5f_1$ should be reliably modeled; 3) in Section VI.A, the instability mode is only identified at the RE AC terminal, whereas part of cases of k_{pvdc} tuning can be analyzed at both AC and DC terminals of the same end (RE) but is no longer feasible for the AC SE terminal. Thus, the independent black-box analyses are invalid for the (inter)harmonics of i_{vsa}, which is explained as a phenomenon of harmonic balance; therefore, "impedance interaction" between
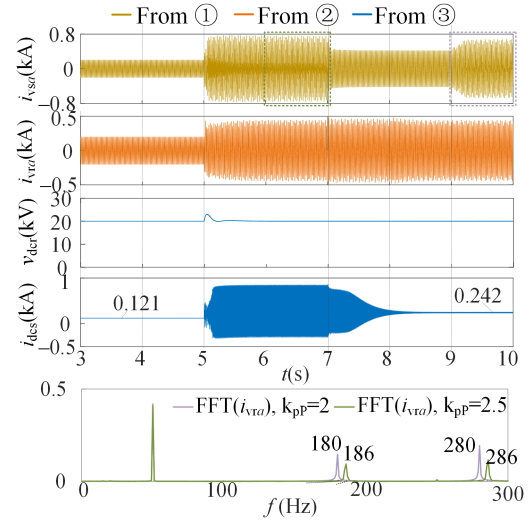

Fig. 17. Time domain simulation with the FFTs (case c).

multiterminal for stability modeling and instability positioning in future privacy-protected analyses is required. The instability source of the studied $h_{\text{vdc}}(s)$ tuning cases is positioned at RE with the DC control loop to be improved as a priority to avoid the unstable mode. The power control can also be selected to tune for $h_{\text{vdc}}(s) = 30+1/0.05s$ when transformers are configured since it acts on the coupling between AC and DC terminals.
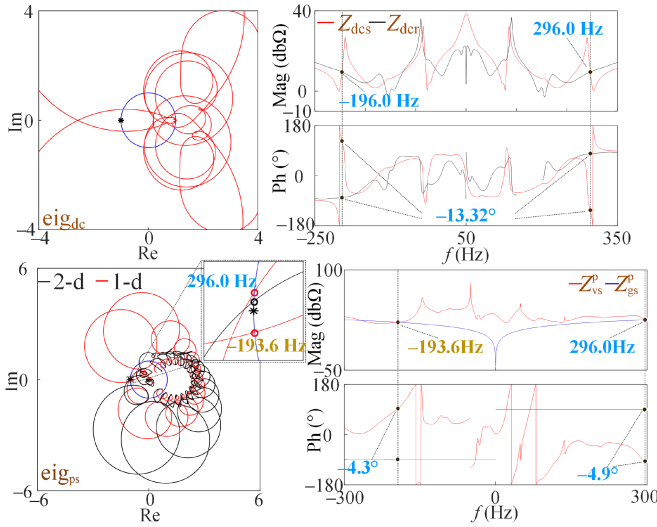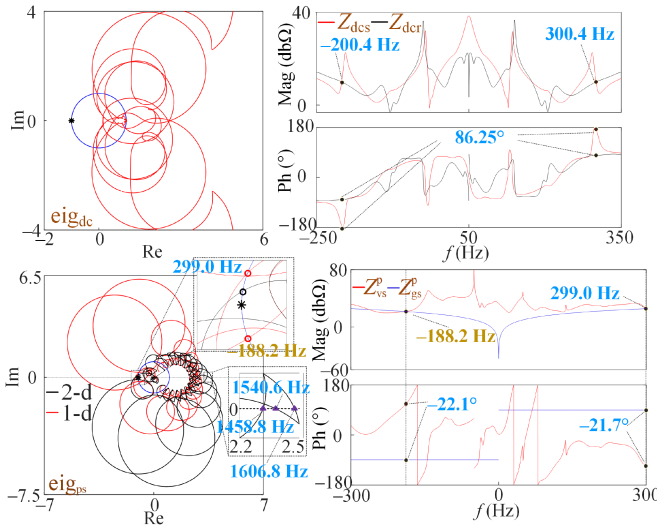
C. Case C: Step of P

Finally, as a practical concern, the stability of P steps from 0.5 pu to 1 pu is analyzed, where L_{gs}^{*} is changed to 10 mH to emulate a weak grid. A group of heuristic simulations is given for each subsystem, which has the time logic as follows:

1) At $t = 3$ s, L_{gs} remains at L_{gs}^{*}, k_{pP} is set to 2, and P^{*} is set to 0.5 pu; 2) At $t = 4$ s, k_{pP} becomes 2.5; 3) At $t = 5$ s, P^{*} steps to 1 pu; 4) At $t = 7$ s, L_{gs} becomes 0; 5) At $t = 8$ s, k_{pP} becomes 2; 6) At $t = 9$ s, L_{gs} turns to L_{gs}^{*}. Fig. 17 shows that $k_{\text{pP}} = 2$ or 2.5 cause the system to be unstable when $P^{*} = 1$ pu on the premise that only subsystem ② cannot stably operate; the frequency of sustained oscillation increases with a larger k_{pP} ($|f_{\text{P}}-f_1| = 230$ Hz and 236 Hz when $k_{\text{pP}} = 2$ and 2.5).

Nevertheless, the frequency domain analyses using Figs. 18 and 19 illustrate that the same unstable mode can be identified at both DC and AC SE terminals when $k_{\text{pP}} = 2$ but can only be identified at the AC SE terminal when $k_{\text{pP}} = 2.5$, while the instabilities cannot be determined at the AC RE terminal (the simulation is disregarded). The model frequency increases from 296 Hz to 299 Hz while PM decreases from –4.9° to –21.7°, which satisfies Fig. 17.

Case c verifies the previous finding that supposing a specified terminal as the instability source for analysis can leave out the authentic unstable mode. Regarding the adaptivity of the simplified AC stability criteria for MMC from TL-VSC, more interesting results are noted. First, the extra unstable modes

Fig. 18.   Nyquist and bode plots ($k_{pP} = 2$).

Fig. 19.   Nyquist and bode plots ($k_{pP} = 2.5$).
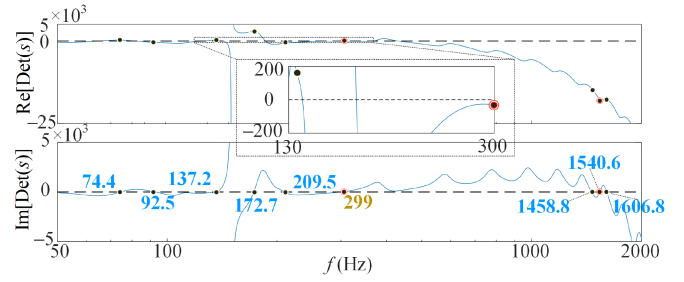

Fig. 20.   Validation of the practical criterion [27] in the MMC-BTB systems considering the nonignorable time delay.

the time delay, as shown by the purple triangles in Fig. 19. Overall, the 2-d Nyquist criterion is essential for AC stability analyses of MMC-BTB systems.

VII.   CONCLUSION

By focusing on an MMC-BTB system, this article discusses several issues in extending the impedance-based analysis from a single MMC to multiterminal systems. Based on theoretical analyses and validations, the following conclusions are drawn:

1) A numerical method is proposed to rapidly and accurately obtain the system steady-state harmonic regardless of whether transformers are configured, which helps unify the complete small-signal stability analysis in the frequency domain.

2) By clarifying the modeling concept, a generalized framework is provided to develop AC/DC TIMs uniformly and succinctly based on the typical control loops and the pure time delay in particular and is verified via frequency scans.

3) Sensitivity analyses are used to emphasize the essential effects of the nonideal transformer and ZSCC on the impedance characteristics, while the rationality of a novel simplified AIM considering NS current control is comparatively studied.

4) Multiple case studies collectively confirm the necessity of executing AC/DC stability analyses with detailed IMs. The unstable mode can be identified at the AC or DC terminal of one MMC and the harmonics spread to the entire system. The replacement of the Nyquist criteria with simplified criteria in wideband stability analyses is potentially inaccurate.

Deeply understanding the modeling concept of this article facilitates more complicated device- and system-level impedance-based modeling and analysis. Future studies will focus on the couplings between multiple physical paths and stability identification with unstable subsystems in the multiterminal system.

APPENDIX
DETAILS OF CONTROL STAGE

The basic $\boldsymbol{J}$ can be decomposed according to Fig. 3, The elements not mentioned default 0 and the same below:

PS current control : $\boldsymbol{J}_1^P(s)(x, x) = -0.5(1 + g)\cdot[h_o\cdot h_d](s)$

$\cdot[h_i(s + j(x + g)\omega_1) + jgk_{de}]\cdot 2k_m k_i, x = n \pm 1,$

NS current control : $\boldsymbol{J}_1^n(s)(x, x) = -0.5(1 + g)$

appear in the 1-d PS loop criterion [26] as the red solid lines in the zoom-in of Figs. 18 and 19 show. Since $|f_p-f_1| = 243.6$ Hz or 238.2 Hz deviates from the real 246 Hz or 249 Hz in two cases, it can potentially affect the estimation of sustained oscillation frequency when k_{pP} increases. In fact, the 1-d and 2-d Nyquist criteria are only equivalent in marginal stability judging [26]. Furthermore, a practical determinant (Det(s))-based criterion [27] is examined since the zeros and poles are difficult to obtain for IMs. By extracting a pair of conjugate right-half plane poles from Det(s), a *stable* mode satisfies:

$$0.5\{Im[\text{Det}(s_{zc}+j2\pi)] - Im[\text{Det}(s_{zc}-j2\pi)]\}\cdot Re[\text{Det}(s_{zc})] > 0 \tag{24}$$

In (24), Im(Det(s)) and Re(Det(s)) separate the imaginary and real parts of Det(s), and s_{zc} is the zero-crossing angular frequency of Im(Det(s)). In Fig. 20, when $k_{pP} = 2.5$, the 1540.6 Hz mode is determined to be unstable except for the expected 299 Hz, which is induced by incorrectly handling

$$\cdot [h_o \cdot h_d](s + j2g\omega_1)$$

$$\cdot [h_i(s + j(x - g)\omega_1) - jgk_{de}] \cdot 2k_m k_i, x = n \pm 1,$$

$$\text{CCSC} : \boldsymbol{J}_2^n(s)(x, x) = -0.5(1 - g) \cdot h_d(s)$$

$$\cdot [h_{CCSC}(s + j(x - 2g)\omega_1) - j2gk_{de}] \cdot k_m k_i, x = n \pm 2,$$

$$h_o(s - j\omega_1) = 0.5(1 + e^{-sT_1/4}), h_d(s - j\omega_1) = e^{-sT_d}. \tag{25}$$

The feedforward part of $\boldsymbol{K}$ is formed by two submatrices:

$$\text{PS/NS current control} : \boldsymbol{K}_{1f}^p(s)/\boldsymbol{K}_{1f}^n(s)(x, x) = k_m k_v k_f$$

$$\cdot e^{-\text{ang}(\boldsymbol{v}_v\langle 1 \rangle)} \cdot \{[h_o \cdot h_d](s)/[h_o \cdot h_d](s + j2g\omega_1)\}, x = n \pm 1. \tag{26}$$

The influences on $\Delta \boldsymbol{m}$ contributed by PLL are divided into:

$$\text{PS current control} : \boldsymbol{K}_{1PLL}^p(x, y)(s) = w \cdot [h_{PLL}^i(s) + h_{PLL}^m(s)$$

$$+ h_{PLL}^{v_v}(s)] \cdot h_{PLL}(s), x = n \pm 1, y = n \pm 1,$$

$$\text{NS current control} : \boldsymbol{K}_{1PLL}^n(x, y)(s) = w \cdot [h_{PLL}^i(s) + h_{PLL}^{v_v}(s)]$$

$$\cdot h_{PLL}(s), x = n \pm 1, y = n \pm 1,$$

$$\text{CCSC} : \boldsymbol{K}_{2PLL}^n(x, y)(s) = w \cdot [h_{PLL}^m(s)]$$

$$\cdot h_{PLL}(s), x = n \pm 2, y = n \pm 1,$$

$$w = 0.5 \cdot (x - n) \cdot l \cdot \text{sign}[(x - n) \cdot (y - n)],$$

$$h_{PLL}^m(s) = -2\boldsymbol{m} \langle |x - n| \rangle,$$

$$h_{PLL}^{v_v}(s + jg(x - n)\omega_1) = -k_m k_f k_v \cdot 2\boldsymbol{v}_v \langle |x - n| \rangle$$

$$\cdot [h_o \cdot h_d](s),$$

$$h_{PLL}^i(s + jg(x - n)\omega_1) = 2k_m k_i \cdot 2\boldsymbol{i} \langle |x - n| \rangle$$

$$\cdot [h_o \cdot h_d](s) \cdot [h_i(s) - jg \cdot (x - n)k_{de}]. \tag{27}$$

$\Delta \boldsymbol{d}$ and $\Delta \boldsymbol{q}$ are different for each end as ($x = n$, $y = n\pm1$):

$$\Delta \boldsymbol{d}_r = \text{diag}[h_d(s + jg(x - n)\omega_1)] \cdot \boldsymbol{U} \cdot \Delta \boldsymbol{v}_{dc},$$

$$\Delta \boldsymbol{q}_r = \text{diag}[h_d(s + jg(x - n)\omega_1)] \cdot \boldsymbol{R} \cdot \Delta \boldsymbol{v}_1,$$

$$\Delta \boldsymbol{d}_s = \text{diag}\{[h_o \cdot h_d](s + jg(x-n)\omega_1)\} \cdot (\boldsymbol{S}\Delta \boldsymbol{v}_1 + \boldsymbol{T}\Delta \boldsymbol{i}),$$

$$\Delta \boldsymbol{q}_s = \text{diag}\{[h_o \cdot h_d](s + jg(x - n)\omega_1)\}$$

$$\cdot (\boldsymbol{W}\Delta \boldsymbol{v}_1 + \boldsymbol{V}\Delta \boldsymbol{i}),$$

$$\boldsymbol{W}(x, y) = j6g\boldsymbol{i} \langle -(y-n) \rangle /k_a, \boldsymbol{V}(x, y) = -j3g\boldsymbol{v}_v \langle -(y-n) \rangle,$$

$$\boldsymbol{S}(x, y) = -6\boldsymbol{i} \langle -(y-n) \rangle /k_a, \boldsymbol{T}(x, y) = -3\boldsymbol{v}_v \langle -(y-n) \rangle,$$

$$\boldsymbol{R}(x, y) = 1.5[e^{-(s-j\omega_1)T_1} - 1] \cdot \boldsymbol{v}_v \langle -(y-n) \rangle /[V_b \cdot (s-j\omega_1)T_1]. \tag{28}$$

$\boldsymbol{E}$ and $\boldsymbol{F}$ are given for each end as ($x = n$):

$$\boldsymbol{E}_r(s)(x, x) = k_{v_{dc}}k_m \cdot [h_{v_{dc}} \cdot h_i](s - j\omega_1),$$

$$\boldsymbol{E}_s(s)(x, x) = k_{PQ}k_m \cdot [h_{PQ} \cdot h_i](s - j\omega_1),$$

$$\boldsymbol{F}_r(s)(x, x) = -jgk_{v_{RMS}}k_m \cdot [h_{v_{RMS}} \cdot h_i](s - j\omega_1),$$

$$\boldsymbol{F}_s(s)(x, x) = -jgk_{PQ}k_m \cdot [h_{PQ} \cdot h_i](s - j\omega_1). \tag{29}$$

$\boldsymbol{B}_i, \boldsymbol{B}_{vdc}$, and $\boldsymbol{B}_{vv}$ are expressed for each end as:

$$\boldsymbol{B}_{v_{dc}r} = -\boldsymbol{E}''_r, \boldsymbol{B}_{ir} = -\boldsymbol{J}, \boldsymbol{B}_{v_vr} = -(\boldsymbol{K} + \boldsymbol{F}''_r \boldsymbol{R}), \boldsymbol{B}_{v_{dc}s} = \boldsymbol{O},$$

$$\boldsymbol{B}_{is} = -[\boldsymbol{J} + (\boldsymbol{F}'_s \boldsymbol{V} + \boldsymbol{E}'_s \boldsymbol{T})/k_a],$$

$$\boldsymbol{B}_{v_vs} = -(\boldsymbol{K} + \boldsymbol{F}'_s \boldsymbol{W} + \boldsymbol{E}'_s \boldsymbol{S}). \tag{30}$$

where the double (single) apostrophe means to integrate the matrices with $h_d(s)$ ($[h_o \cdot h_d](s)$) of $\Delta \boldsymbol{d}$ or $\Delta \boldsymbol{q}$ into $\boldsymbol{E}$ or $\boldsymbol{F}$.

REFERENCES

[1] A. Lesnicar and R. Marquardt, "An innovative modular multilevel converter topology suitable for a wide power range," in *Proc. IEEE Bologna Power Tech Conf.*, 2003, vol. 3, pp. 1–6.

[2] J. Lyu, X. Cai, and M. Molinas, "Frequency domain stability analysis of MMC-based HVdc for wind farm integration," *IEEE J. Emerg. Sel. Topics Power Electron.*, vol. 4, no. 1, pp. 141–151, Mar. 2016.

[3] C. Zou et al., "Analysis of resonance between a VSC-HVDC converter and the AC grid," *IEEE Trans. Power Electron.*, vol. 33, no. 12, pp. 10157–10168, Dec. 2018.

[4] Y. Li, T. An, D. Zhang, X. Pei, K. Ji, and G. Tang, "Analysis and suppression control of high frequency resonance for MMC-HVDC system," *IEEE Trans. Power Del.*, vol. 36, no. 6, pp. 3867–3881, Dec. 2021.

[5] Z. Xu, B. Li, S. Li, X. Wang, and D. Xu, "MMC admittance model simplification based on signal-flow graph," *IEEE Trans. Power Electron.*, vol. 37, no. 5, pp. 5547–5561, May 2022.

[6] Z. Xu, B. Li, S. Wang, S. Zhang, and D. Xu, "Generalized single-phase harmonic state space modeling of the modular multilevel converter with zero-sequence voltage compensation," *IEEE Trans. Ind. Electron.*, vol. 66, no. 8, pp. 6416–6426, Aug. 2019.

[7] T. Xue, J. Lyu, H. Wang, and X. Cai, "A complete impedance model of a PMSG-based wind energy conversion system and its effect on the stability analysis of MMC-HVDC connected offshore wind farms," *IEEE Trans. Energy Convers.*, vol. 36, no. 4, pp. 3449–3461, Dec. 2021.

[8] H. Wu and X. Wang, "Dynamic impact of zero-sequence circulating current on modular multilevel converters: Complex-valued AC impedance modeling and analysis," *IEEE J. Emerg. Sel. Topics Power Electron.*, vol. 8, no. 2, pp. 1947–1963, Jun. 2020.

[9] S. Zhu et al., "Stability assessment of modular multilevel converters based on linear time-periodic theory: Time-domain vs. frequency-domain," *IEEE Trans. Power Del.*, vol. 37, no. 5, pp. 3980–3995, Oct. 2022.

[10] P. De Rua and J. Beerten, "Generalization of harmonic state-space framework to delayed periodic systems for stability analysis of the modular multilevel converter," *IEEE Trans. Power Del.*, vol. 37, no. 4, pp. 2661–2672, Aug. 2022.

[11] J. Sun and H. Liu, "Sequence impedance modeling of modular multilevel converters," *IEEE J. Emerg. Sel. Topics Power Electron.*, vol. 5, no. 4, pp. 1427–1443, 2017.

[12] K. Ji, G. Tang, H. Pang, and J. Yang, "Impedance modeling and analysis of MMC-HVDC for offshore wind farm integration," *IEEE Trans. Power Del.*, vol. 35, no. 3, pp. 1488–1501, Jun. 2020.

[13] K. Ji et al., "Generalized impedance analysis and new sight at damping controls for wind farm connected MMC–HVdc," *IEEE J. Emerg. Sel. Topics Power Electron.*, vol. 9, no. 6, pp. 7278–7295, Dec. 2021.

[14] T. Roose, A. Lekic, M. M. Alam, and J. Beerten, "Stability analysis of high-frequency interactions between a converter and HVDC grid resonances," *IEEE Trans. Power Del.*, vol. 36, no. 6, pp. 3414–3425, Dec. 2021.

[15] T. Yin et al., "Impedance-based characterization of positive-negative sequence separation and its effects on MMC-HVDC stability," *IEEE J. Emerg. Sel. Topics Power Electron.*, vol. 10, no. 4, pp. 4395–4412, Aug. 2022.

[16] T. Huang, F. Yang, D. Zhang, and X. Chen, "High-frequency stability analysis and impedance optimization for an MMC-HVDC integrated system considering delay effects," *IEEE J. Emerg. Sel. Topics Circuits Syst.*, vol. 12, no. 1, pp. 59–72, Mar. 2022.

[17] J. Segundo-Ramirez, A. Bayo-Salas, M. Esparza, J. Beerten, and P. Gómez, "Frequency domain methods for accuracy assessment of wideband models in electromagnetic transient stability studies," *IEEE Trans. Power Del.*, vol. 35, no. 1, pp. 71–83, Feb. 2020.

[18] Y. Xu, H. Nian, and L. Chen, "Small-signal modeling and analysis of DC-link dynamics in type-IV wind turbine system," *IEEE Trans. Ind. Electron.*, vol. 68, no. 2, pp. 1423–1433, Feb. 2021.

[19] J. Sun, "Two-port characterization and transfer immittances of AC-DC converters—Part I: Modeling," *IEEE Open J. Power Electron.*, vol. 2, no. 10, pp. 440–462, Aug. 2021.

[20] J. Man, L. Chen, V. Terzija, and X. Xie, "Mitigating high-frequency resonance in MMC-HVDC systems using adaptive notch filters," *IEEE Trans. Power Syst.*, vol. 37, no. 3, pp. 2086–2096, May 2022.

[21] F. Zhao, G. Xiao, and T. Zhao, "Accurate steady-state mathematical models of arm and line harmonic characteristics for modular multilevel converter," *IEEE Trans. Power Del.*, vol. 33, no. 3, pp. 1308–1318, Jun. 2018.

[22] K. Ilves, S. Norrga, L. Harnefors, and H. Nee, "On energy storage requirements in modular multilevel converters," *IEEE Trans. Power Electron.*, vol. 29, no. 1, pp. 77–88, Jan. 2014..

[23] P. Khamphakdi, K. Sekiguchi, M. Hagiwara, and H. Akagi, "A transformerless back-to-back (BTB) system using modular multilevel cascade converters for power distribution systems," *IEEE Trans. Power Electron.*, vol. 30, no. 4, pp. 1866–1875, Apr. 2015.

[24] Ö. C. Sakinci, A. Lekić, and J. Beerten, "Generalized impedance-based AC/DC power system modeling for harmonic stability analysis," *Int. J. Elect. Power*, vol. 143, Dec. 2022, Art. no. 108456.

[25] Y. Liao, H. Wu, X. Wang, M. Ndreko, R. Dimitrovski, and W. Winter, "Stability and sensitivity analysis of multi-vendor, multi-terminal HVDC systems," *IEEE Open J. Power Electron.*, vol. 4, pp. 52–66, Jan. 2023.

[26] C. Zhang, X. Cai, A. Rygg, and M. Molinas, "Sequence domain SISO equivalent models of a grid-tied voltage source converter system for small-signal stability analysis," *IEEE Trans. Energy Convers.*, vol. 33, no. 2, pp. 741–749, Jun. 2018.

[27] H. Liu, X. Xie, and W. Liu, "An oscillatory stability criterion based on the unified dq-frame impedance network model for power systems with high-penetration renewables," *IEEE Trans. Power Syst.*, vol. 33, no. 3, pp. 3472–3485, May 2018.

[28] R. Li, J. E. Fletcher, and B. W. Williams, "Influence of third harmonic injection on modular multilevel converter-based high-voltage direct current transmission systems," *IET Gener., Transmiss. Distrib.*, vol. 10, no. 11, pp. 2764–2770, Aug. 2016.

Chongbin Zhao (Student Member, IEEE) received the B.S. degree in electrical engineering in 2019 from Tsinghua University, Beijing, China, where he is currently working toward the Ph.D. degree. Since January 2023, He has also been a Visiting Scholar with Rensselaer Polytechnic Institute, Troy, NY, USA. His research interests include power quality analysis and control, and emerging converter-driven power system stability analysis and control.

Qirong Jiang received the B.S. and Ph.D. degrees in electrical engineering from Tsinghua University, Beijing, China, in 1992 and 1997, respectively. In 1997, he was a Lecturer with the Department of Electrical Engineering, Tsinghua University, where he later became an Associate Professor in 1999. Since 2006, he has been a Professor. His research interests include power system analysis and control, modeling and control of flexible ac transmission systems, power-quality analysis and mitigation, power-electronic equipment, and renewable energy power conversion.